

Review

# Quartz-Enhanced Photoacoustic Spectroscopy in the Terahertz Spectral Range

Alexey P. Votintsev <sup>1</sup>, Alexey V. Borisov <sup>1</sup>, Didar R. Makashev <sup>1</sup>, Mariya Y. Stoyanova <sup>1</sup> and Yury V. Kistenev <sup>1,2,\*</sup> 

<sup>1</sup> Laboratory of Biophotonics, National Research Tomsk State University, Tomsk 634050, Russia; vleksei1810@mail.tsu.ru (A.P.V.); borisov@phys.tsu.ru (A.V.B.); didar.makashev@mail.tsu.ru (D.R.M.); mariya.stoyanova@mail.tsu.ru (M.Y.S.)

<sup>2</sup> V.E. Zuev Institute of Atmospheric Optics SB RAS, Tomsk 634055, Russia

\* Correspondence: yuk@iao.ru

**Abstract:** Infrared laser photo-acoustic spectroscopy provides very high sensitivity of a gas sample analysis when high-power tunable laser radiation sources and resonant photo-acoustic detectors (PADs) are used. In the resonant PAD, the acoustic signal generated by absorbed laser radiation in a measurement chamber is amplified proportionally to a Q-factor of the acoustic resonator. But, compact tunable high-power lasers (with power above 100 mW) still are not widely spread in the terahertz spectral range. One of the ways to achieve an acceptable sensitivity of terahertz photo-acoustic spectroscopy is using PADs with a very high Q-factor. The latter can be achieved using PAD with a quartz tuning fork. The current state in this field is presented in the review.

**Keywords:** photo-acoustic spectroscopy; resonant photo-acoustic detector; Q-factor; quartz tuning fork; quartz-enhanced photoacoustic spectroscopy

## 1. Introduction

An absorption spectroscopy is based on the effect of resonant absorption of optical radiation by a target molecule. Among such methods, the laser photo-acoustic spectroscopy (PAS) is one of the most sensitive ones. PAS is based on registering the acoustic wave appearing in a measurement chamber with a studied gas sample absorbing the periodically modulated optical/laser light, either by amplitude or wavelength. By varying the optical/laser light wavelength, we can measure an absorption spectrum shape of the gas sample. The advantages of laser PAS compared to Bouguer's law-based spectroscopy are the following: low-cost and simple implementation; the useful signal registered by a mechanical resonator not a photonic detector; and removing specific restrictions related to the latter, such as nonuniform spectral response, shot noise, and flicker noise. Also, amplitude of the acoustic wave registered by the mechanical resonator is defined by optical radiation power that removes the requirement for measurement chamber length, which is important for Bouguer's law-based spectrometers [1]. These benefits make it attractive to use infrared (IR) PAS for express local control of pollution or greenhouse gases in the ground atmosphere [2]. Terahertz (THz) PAS also can be used for this goal. Presented in the HITRAN [3] and GEISA spectroscopic databases [4], molecules of interest in the atmosphere environmental monitoring tasks have absorption lines in the THz spectral range are as follows [5]:

- Sulfur-containing compounds (carbonyl sulfide—COS, carbon disulfide—CS<sub>2</sub>, hydrogen sulfide—H<sub>2</sub>S, sulfur oxide—SO<sub>2</sub>);
- Halocarbons (chloromethane—CH<sub>3</sub>Cl);
- Nitrogen-containing compounds (chlorine nitrate—ClONO<sub>2</sub>, ammonia—NH<sub>3</sub>, nitric oxide—N<sub>2</sub>O, nitric acid—HNO<sub>3</sub>);
- Volatile organic compounds (methanol—CH<sub>3</sub>OH, methane—CH<sub>4</sub>, ethane—C<sub>2</sub>H<sub>6</sub>).



**Citation:** Votintsev, A.P.; Borisov, A.V.; Makashev, D.R.; Stoyanova, M.Y.; Kistenev, Y.V. Quartz-Enhanced Photoacoustic Spectroscopy in the Terahertz Spectral Range. *Photonics* **2023**, *10*, 835. <https://doi.org/10.3390/photonics10070835>

Received: 11 June 2023

Revised: 13 July 2023

Accepted: 16 July 2023

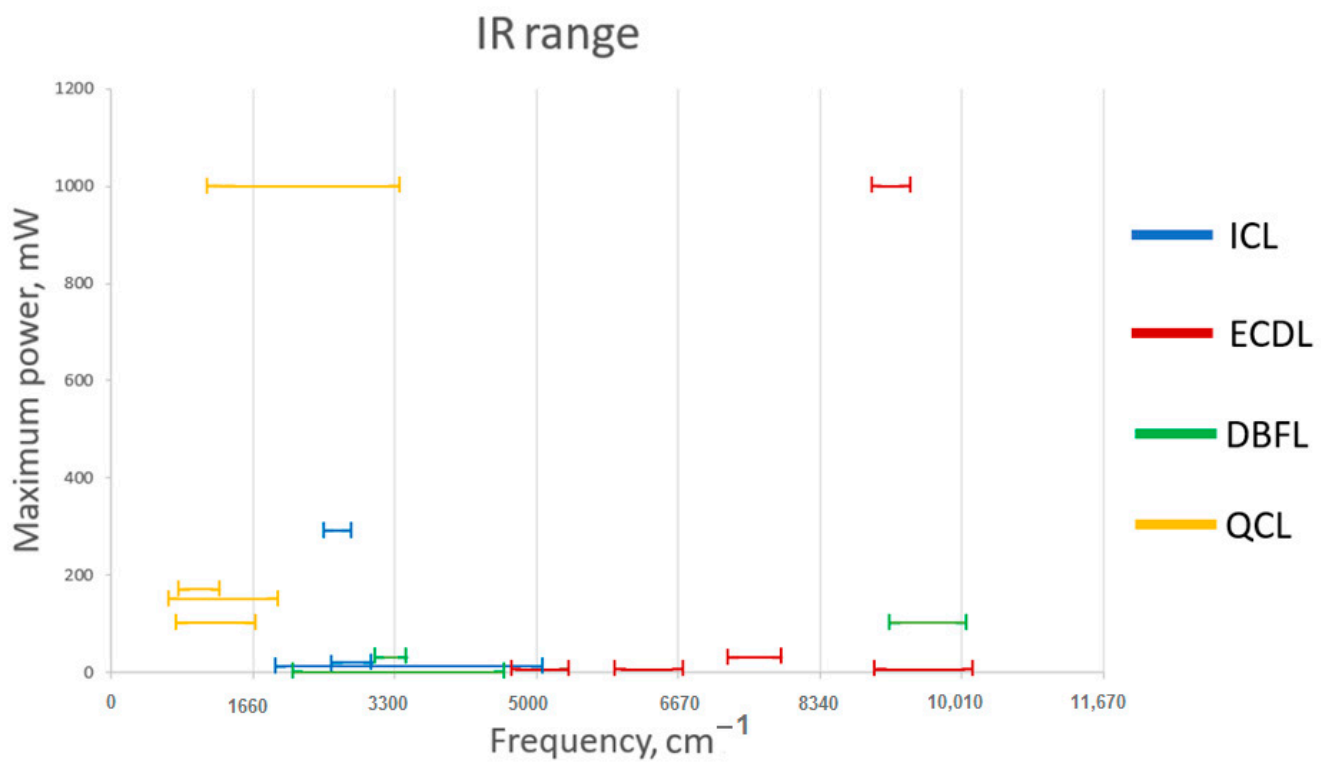
Published: 19 July 2023



**Copyright:** © 2023 by the authors. Licensee MDPI, Basel, Switzerland. This article is an open access article distributed under the terms and conditions of the Creative Commons Attribution (CC BY) license (<https://creativecommons.org/licenses/by/4.0/>).

The outstanding measurements presented in the atmosphere with non-polar molecule ( $\text{CH}_4$  and  $\text{N}_2\text{O}$ ) detection in the sub-THz spectral range by a Bouguer’s law-based spectrometer with a multi-pass measurement chamber were conducted [6]. Methane was analyzed in a White-type chamber with absorption path length of 20 m. A Chernin-type chamber with a 200 m path length was used for  $\text{N}_2\text{O}$  detection. To avoid absorption lines that overlap owing to the impact broadening, the authors worked with mbar pressures in the chamber. The adjustment of such a multi-pass measurement chamber is a non-trivial task.

PAS requires sources with periodically varied amplitude or frequency (wavelength) of optical radiation. In the IR spectral range, two options of the photo-acoustic detector (PAD) chamber design are used. In a non-resonant PAD, the frequency of optical wave amplitude (or frequency) modulation is lower than the measurement chamber acoustic resonance frequencies. In the resonant PAD, these frequencies coincide, the chamber works as an acoustic resonator, and the acoustic signal is increased proportionally to the Q-factor of the acoustic resonator. Helmholtz resonators, including differential Helmholtz resonators, one-dimensional cylindrical resonators, and volumetric resonators, are often used in resonant IR PADs [7–10]. The Q-factor of such PADs can achieve several hundred [9]. Since the photo-acoustic (PA) signal is proportional to the optical radiation energy absorbed by the gas sample, the powerful laser radiation sources are preferable. In the IR spectral range, many powerful wavelength-tunable laser radiation sources are in the market. For example, typical optical parametric oscillators provide optical power from several hundred mW to units of watts and a spectral tuning range from about 2  $\mu\text{m}$  to about 10  $\mu\text{m}$  [11]. Fast progress in semiconductor laser development makes them very attractive in spectroscopy applications. Comparison of various types of such lasers in the IR and THz spectral ranges is presented in Figure 1 [12–34].



(a)

Figure 1. Cont.

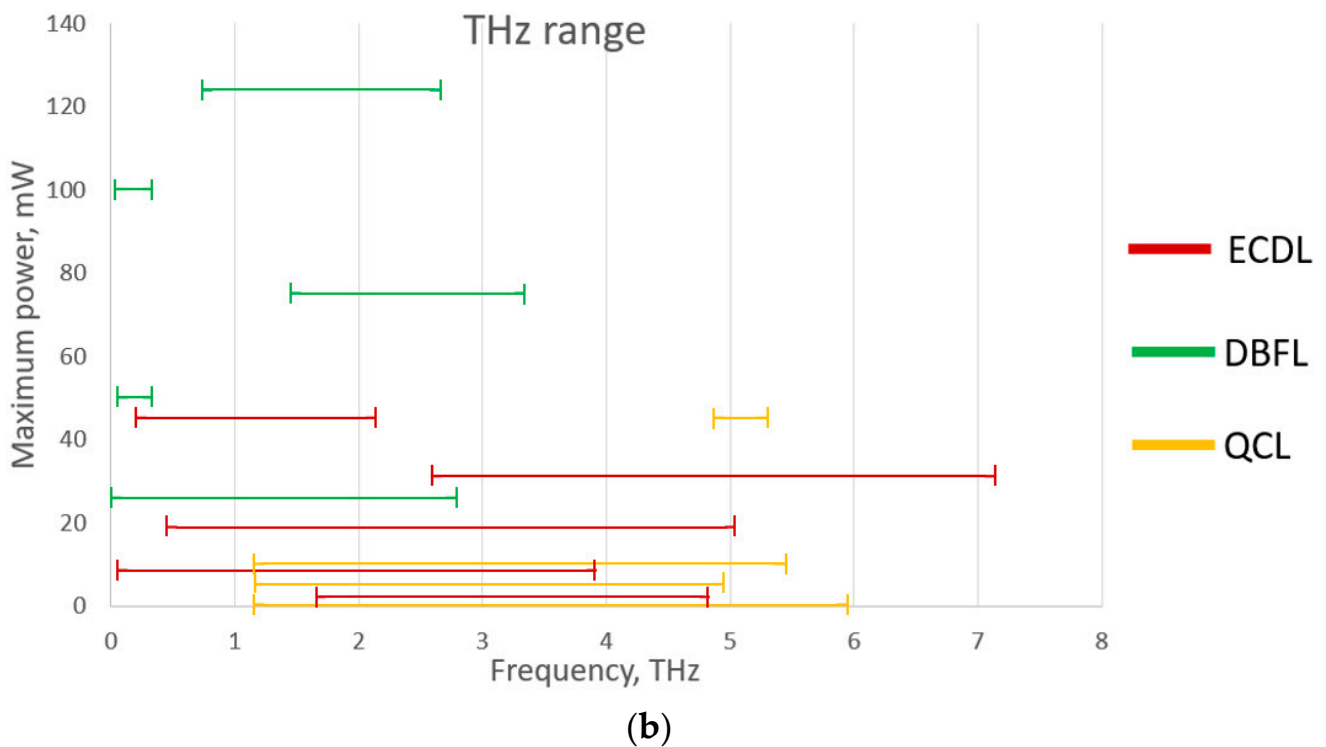


**Figure 1.** Comparison of power and spectral tunability of various types of semiconductor lasers working in the IR (a) and THz (b) spectral ranges. Here, ICL means inter-band cascade laser, ECDL is external-cavity diode laser, DBFL is distributed feedback diode laser, QCL is quantum cascade laser.

It follows that compact tunable high-power lasers (with power above 100 mW) still are not widely spread in the THz spectral range. One of the ways to improve the sensitivity of a THz PAD is to increase the Q-factor of the resonator. The drawback of standard IR PAD constructions is a relatively small Q-factor value [35]. An alternative is the quartz tuning fork (QTF). Quartz has been widely used for resonant acoustic transduction because it combines good mechanical properties and displays a strong piezoelectric effect. The latter provides a high efficiency of conversion of an acoustic signal to an electrical current. QTF is a base of quartz enhanced photo-acoustic spectroscopy (QEPAS). The independence of the QTF converter from the optical radiation wavelength makes QEPAS rather universal, which makes it possible to explore different spectral ranges by simply replacing the optical radiation source. QEPAS THz devices can possess the following benefits: compactness, sensitivity, the ability to work in a wide spectral range, and the ability to work in the field.

Another benefit of using QTF in the THz spectral range is associated with a fast transformation of absorbed energy of optical radiation into the heat: The rotational-translation relaxation time is up to three orders of magnitude smaller compared to vibrational-translation relaxation time [36]. The latter is the key factor of the efficiency of QEPAS because faster relaxation often means a higher signal while it allows working at a low pressure. Benefits of the latter are described below.

This review presents the current state in the development of QTF-based THz PADs, as well as the design and technical parameters of THz QEPAS devices.

## 2. QTF-Based THz PAD Design

The main element of the QEPAS is a QTF placed inside a measurement chamber, which can have an open construction. A typical QTF design is presented in Figure 2.

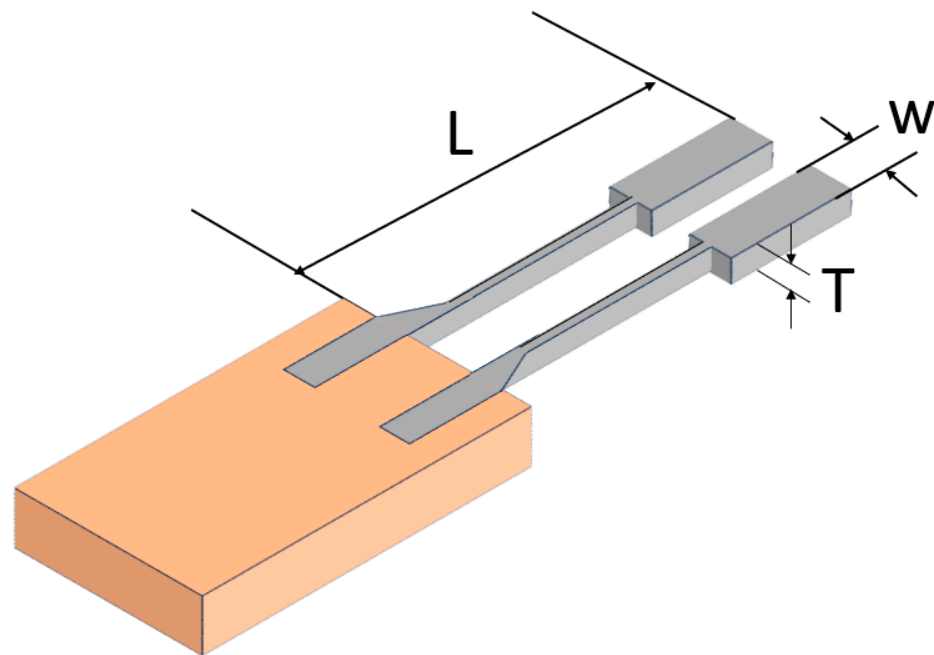


**Figure 2.** Typical QTF design. Here,  $L$ ,  $W$ ,  $T$  are the prong length, width, and thickness, correspondingly.

Such QTF operates like a standard tuning fork in regard to the acoustic resonance frequency and Q-factor [37,38]. Owing to the piezoelectric effect, the QTF prongs oscillate when an external alternating voltage is applied. An inverse piezoelectric effect is used in a gas sample spectral analysis with QTF when the following conditions are fulfilled:

- The optical radiation wave is focused between QTF prongs;
- The wavelength of optical radiation is close to the wavelength of an absorption line of a molecular component of a studied gas sample;
- The optical radiation wave amplitude (or wavelength) is modulated with a frequency coinciding with the frequency of an acoustic resonance of QTF;

Then, the temperature of the gas sample is changed periodically, and an acoustic wave appears, providing forced fluctuations of the QTF prongs with a “large” amplitude owing to the resonance condition. In the result, owing to the inverse piezoelectric effect, the QTF generates alternating current proportional to the absorbing molecular component concentration. When an optical radiation wave is focused between QTF prongs, an acoustic noise does not affect essentially on the useful signal. The reasons are a  $1/f$  noise is very low at typical frequencies of the QTF acoustic resonances (several kHz), and a narrow peak of the acoustic resonance curve allows one to select useful spectral components in a total electrical signal on the QTF output [39].

The most important features of QTF are the frequency of acoustic resonance  $\omega_0$  and the Q-factor, which determines the acoustic resonance width  $\Delta\omega$ :

$$Q = \frac{\omega_0}{\Delta\omega} \tag{1}$$

The Q-factor value is defined by the several physical effects:

$$\frac{1}{Q} = \frac{1}{Q_V} + \frac{1}{Q_T} + \frac{1}{Q_S} + \frac{1}{Q_A} \tag{2}$$

where  $Q_V$  describes viscosity dissipation,  $Q_T$ ,  $Q_S$ , and  $Q_A$  describe thermoelastic, a fork support system, and acoustic losses, respectively [40]. The authors pointed out the following:

- Using the isothermal regime for “thin” prongs and using the adiabatic regime for “thick” prongs reduces  $Q_T$ ;
- $Q_A$  increases with the prong width  $T$  increasing and the thickness  $W$  decreasing;

- $Q_S$  is inversely proportional to  $(L/W)^3$ ;
- $Q_A$  is defined by the friction force arising at the prong–ambient gas boundary, which depends on the prong shape.

The Q-factor depends on QTF geometrical parameters as follows [41]:

$$Q = 3.78 \cdot 10^5 \frac{WT}{L} \tag{3}$$

Combining the ideal gas law, the kinetic theory of gases, and the Bouguer’s law, the pressure change  $\Delta p$  near the prong per optical radiation variation period can be presented in the form [42]:

$$\Delta p = \frac{P_0 p_x \alpha l}{3V f_m} = \frac{P_0 \alpha p_x}{3\pi r^2 f_m} \tag{4}$$

where  $P_0$  is the power of the optical wave at the input of the measurement chamber,  $\alpha$  is the absorption coefficient,  $f_m$  is the frequency of an optical radiation amplitude modulation,  $p_x$  is the partial pressure of the gas component under study,  $l$ ,  $r$ ,  $V$  are the length, radius, and volume of the measurement chamber, correspondingly. This formula emphasizes an importance of using high-power radiation sources. But, there are other ways to enhance an electrical signal on the PAD output. In common, the PA signal is defined by  $Q\Delta p$  multiplication [43,44]. Therefore, the efficiency of transformation of optical radiation energy into an electrical signal by PAD is directly related to the Q-factor value.

The frequency of the prong acoustic resonance can be evaluated by modeling its vibrations by a harmonic oscillator with damping and external harmonic forces using the Newton’s second law for stationary conditions when all internal and external forces acting on the prong are balanced [45]. However, considering the prong as a system with distributed parameters allows taking into account the peculiarities of action of inertial, elastic, and dissipative forces in the PA effect [41]. The Euler–Bernoulli theory gives a fork prong resonance frequency in vacuum  $f_{n,vac}$  as follows [46,47]:

$$f_{n,vac} = \frac{\pi T}{8\sqrt{12}L^2} \sqrt{\frac{E}{\rho}} v_n^2 \tag{5}$$

where  $T$ ,  $L$  are the prong thickness and length,  $\rho = 2650 \text{ kg/m}^3$  is the quartz density,  $E = 72 \text{ GPa}$  is the quartz Young’s modulus, and the  $n$  index enumerates vibration modes:  $v_0 = 1.194$  for the lowest bending vibration mode (the fundamental mode) and  $v_1 = 2.988$  for the first overtone mode (see Figure 3). The accuracy of Equation (5) is quite high; the discrepancy between calculated and measured  $v_n$  values was below 3.2% [36].

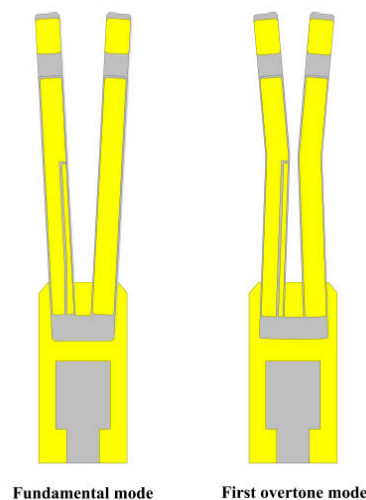


Figure 3. QTF fundamental and the first overtone flexural modes [35].

Validation of this approach was conducted with a custom fork manufactured using a silicon plate on an insulator (silicon on insulator, SOI) [41]. The Plasma-Therm Versaline deep reactive ion etch system was used to etch gaps of 3–8  $\mu\text{m}$  in the layer of the SOI sample to form the fork. A reflective Ti/Au layer (20/100 nm) was deposited at the end of the prong to provide interferometric measurements of the PA signal. The authors recorded the absorption spectrum of methyl cyanide in the 311.72–312.79 GHz range at a pressure varied from 13 to 400 mTorr. The Q-factor of the created QEPAS was  $\sim 2500$  for 13 mTorr. The ratio of the acoustic signals at pressures 400 and 13 mTorr was approximately equal to 15.

Many QEPAS devices use commercial QTFs having the fundamental bending mode equal to  $\sim 32.76$  kHz. These QTFs are oriented on the electronics market with specific requirements, which are not very optimal for gas sensing [40]. For example, they are characterized by a small volume (typical quartz crystal prong length  $L = 3.0$  mm, thickness  $T = 0.35$  mm, and width  $W = 0.34$  mm) and a distance between the prongs of 300  $\mu\text{m}$  [48]. The latter plays a crucial role in the acoustic–electrical conversion efficiency, since the amplitude of the pressure on the QTF prongs produced by the acoustic wave decreases with increasing the distance between the focus of the optical beam and the inner surface of the prongs. Thus, the distance between prongs should be chosen as small as possible, but simultaneously, hitting the prongs by the optical beam should be avoided. This obstacle restricts the usefulness of commercial QTFs in the THz spectral range owing to the difficulty of a suitable focus of the THz wave between the prongs [46] and stimulates creation of custom QTFs.

To produce a QTF, the authors [38] used a photolithographic method of etching a quartz plate. Chrome/gold contacts were deposited on both sides of the QTF. The overall size of the QTF was 3.3 cm  $\times$  0.4 cm  $\times$  0.8 cm. The gap between the prongs was  $\sim 1$  mm. The first QTF bend frequency ( $f_0$ ) was near 4246 Hz. At atmospheric pressure, the first ( $f_1$ ) and third ( $f_3$ ) bending modes of the QTF were equal to  $f_1 = 4.245$  kHz and  $f_3 = 25.4$  kHz; the Q-factor was  $Q_1 = 13,100$ ,  $Q_3 = 9800$ , respectively.

A custom QTF enclosed in a cylindrical acoustic cavity with longitudinal acoustic micro-resonators was created (see Figure 4) [49]. The QTF had a 2 mm gap between prongs, quite a low frequency of the acoustic resonance (21.23 kHz), and the high Q-factor:  $7.32 \times 10^3$  (without the acoustic cavity) and  $1.27 \times 10^5$  (with the acoustic cavity). The normalized noise equivalent absorption (NNEA) was  $3.7 \times 10^9 \text{ cm}^1 \cdot \text{W} / \sqrt{\text{Hz}}$  for  $\text{CO}_2$  detection at an atmospheric pressure. NNEA is defined as:

$$NNEA = \alpha_{min} P \sqrt{t} \quad (6)$$

where  $\alpha_{min}$  is the minimum detectable absorption coefficient,  $P$  is the optical radiation source power, and  $t$  is the time of accumulation of measurements [42,50].

An experimental and theoretical analysis of the influence of a QTF dimensions on its main physical parameters, including the Q-factor, the acoustic resonance frequency, and electrical resistance, was conducted in [38,47]. The authors created several QTFs suitable for the THz spectral range. These QTFs differed by the prong length (3.5 mm, 10 mm, 11 mm, 17 mm), thickness (0.2 mm, 0.9 mm, 0.5 mm, 1.0 mm), distance between prongs (0.4 mm, 0.8 mm, 0.6 mm, 0.7 mm) for QTF#1–QTF#4, respectively. It is interesting to compare the smallest QTF#1 and the largest QTF#4. The latter also had the largest distance between the prongs. To evaluate parameters of the QTF#4, a special filter having a high cutoff frequency of 50 kHz was used by authors, so only the first  $f_1 = 4.245$  kHz and the third  $f_3 = 25.4$  kHz bending modes were measured. The corresponding Q-factors were  $Q_1 = 13,100$  and  $Q_3 = 9800$  (at atmospheric pressure).

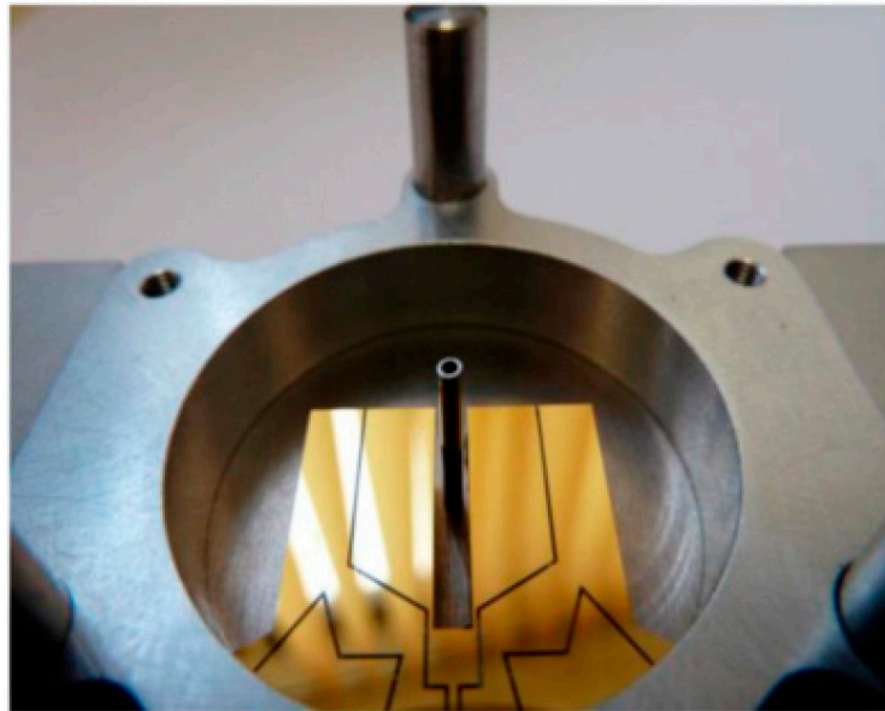


**Figure 4.** A photo of the custom QTF within its cylindrical acoustic cavity with the micro-resonators for acoustic amplification [49].

When using the QTF#4, the minimum detection limit of hydrogen sulfide (H<sub>2</sub>S) was 160 ppb. Here, the minimum detection limit corresponds to minimal concentration of studied gas, which can be registered. A representative frequency response curve measured for QTF#1 at a pressure of 100 Torr in air has the resonance frequency 14,020.14 Hz and resonance curve half width at half maximum (HWHM)—about 1 Hz. At 500 Torr pressure, the Q-factor decreases roughly twice [47]. But, it does not mean that the efficiency of QEPAS increases monotonically with the pressure decreasing. We also should consider that gas pressure  $p$  depends on its density. For example, a maximal PA signal dependent on chamber pressure was at a pressure of about 125 mbar when the measurement of a C<sub>2</sub>H<sub>2</sub> sample is conducted using a cantilever PAD [51].

To avoid overlapping in neighboring lines, we should bear in mind that the absorption line impact broadening decreases with the pressure decreasing. The impact broadening of an absorption line is described by a Lorentz curve with HWHM  $\gamma(p, T)$  equal to

$$\gamma(p, T) = \left(\frac{T_{ref}}{T}\right)^{n_{air}} \left(\gamma_{air}(p_{ref}, T)(p - p_{self}) + \gamma_{self}(p_{ref}, T_{ref})p_{self}\right) \quad (7)$$

where  $p$  is measured in Atm,  $T(K)$  is the temperature in Kelvin,  $p_{self}$  (Atm) is the partial pressure of a definite component,  $n_{air}$  is the coefficient describing the temperature dependence of air broadening,  $\gamma_{self}$ ,  $\gamma_{air}$  is the self-broadening and air-broadening HWHM, respectively; and  $T_{ref}$ ,  $p_{ref}$  is a normal temperature and pressure. Therefore, the optimal choice of pressure in the measurement chamber is a multi-factor task, which needs simulation analysis for a concrete situation.

Additional acoustic micro-resonators in a form of small metallic tubes are often used to enhance the QTF response [35]. The optimum tube length  $L$  lies in the  $\lambda_s/4 < L < \lambda_s/2$  range, where  $\lambda_s$  is the wavelength of the acoustic wave [52].

Another way to improve an efficiency of the conversion of optical radiation power absorbed by the studied gas into the electrical signal is by combing optical and acoustical resonances. Verstuyft M. and co-authors [53] proposed a detector based on a photonic crystal resonator with a cylindrical cavity (modal volume  $1.5 \times 10^4 \mu\text{m}^3$ ). It is closed at

one end by a thin membrane so that it forms a semi-open acoustic resonator, the fundamental frequency of which was 720 kHz. In fact, this detector includes three resonators: The photonic crystal cavity focuses the optical radiation in the cylindrical cavity, which operates as a half-open acoustic resonator, covered by a membrane that functions as an additional mechanical resonator. The concentration of a studied gas can be determined by the amplitude of the membrane motion. Conducted simulation gave an estimate of the detection limit for methanol equal to 1 ppm for the THz radiation source power of 1 mW and an integration time of 25 ms. The estimated  $1/Q = 1/Q_V + 1/Q_T$  value did not exceeded 70.

THz radiation should be located inside the resonator that limits the Q-factor of PAD and sensitivity to the environment. Seems to be that the first off-beam scheme of a QTF PAD, which overcame the standard scheme drawbacks, was suggested in [54]. The off-beam scheme also removes limitations on an optical radiation beam diameter. This scheme provided the NNEA equal to  $5.9 \cdot 10^{-9} \text{ cm}^{-1} \text{ W/Hz}^{1/2}$  for atmospheric water vapor detection [54]. Now, the one-side off-beam scheme is often used [55–57]. An obvious expanding of this idea is to use a double off-beam scheme. The physical principle of operation of such a QTF looks the same as in a standard QTF, where the longitudinal axis of the wave is focused between two prongs. Here, the prongs move symmetrically when a cylindrical acoustic wave is generated. A double off-beam scheme satisfied the same condition, if the acoustic source acts symmetrically on the inner surfaces of both prongs [58]. This scheme is more flexible owing to the absence of requirements on a diameter of optical wave beam but has more complex implementation. This technical problem was solved in [58] using two mirrors placed at an angle of 90 degrees regarding each other (see Figure 5).

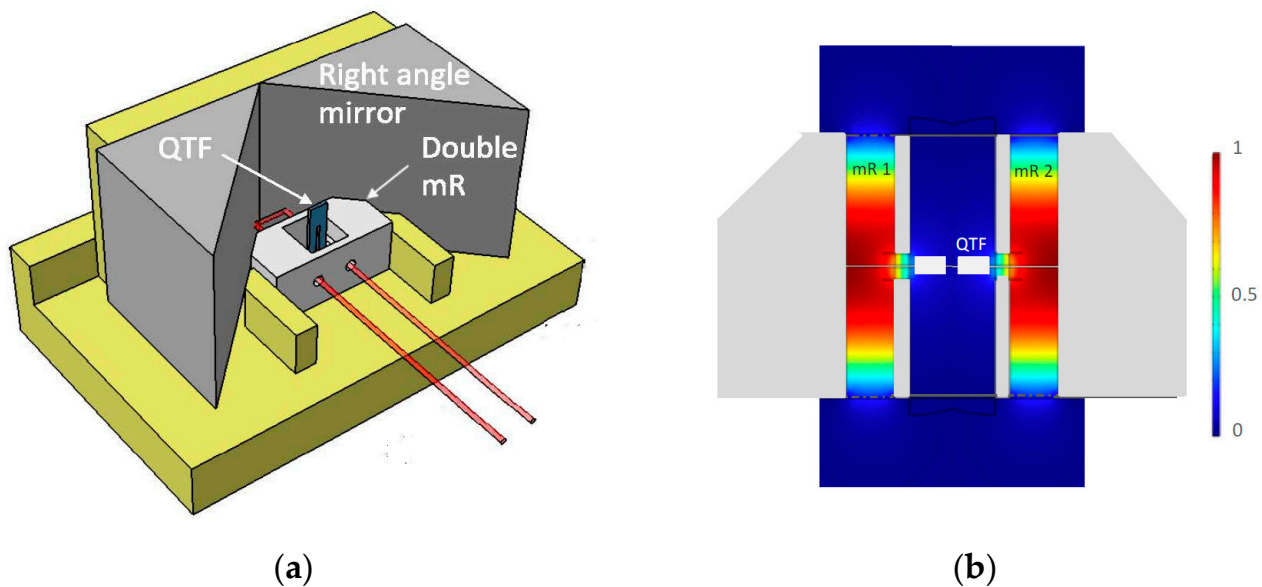


**Figure 5.** QEPAS implementation with double off-beam scheme (a) and normalized acoustic pressure generated near QTF for  $f = 32,815 \text{ Hz}$ , corresponding to its acoustic resonant frequency (b) [58].

Vogt D.V. and co-authors [59,60] used an ultra-high-velocity disc-shape micro-resonator manufactured from high-resistivity float-zone silicon. The disc had a diameter of 12 mm and a thickness of 66  $\mu\text{m}$ . In this construction, the electromagnetic field is located outside the disc in the shape of a damped distribution (Figure 6). This resonator was used for water vapor detection. The measured Q-factor value was in the  $(120\text{--}70) \times 10^3$  interval when water vapor concentration varied from 0 to 140 ppm. The estimated water vapor limit of detection was less than 4 ppm for the measurements carried out at the atmospheric pressure conditions.

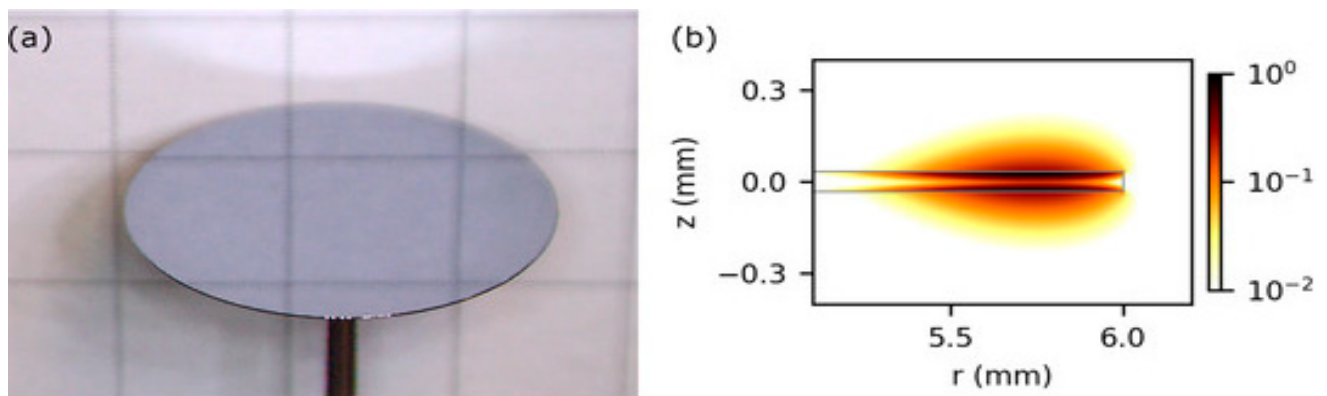


**Figure 6.** The disk micro-resonator (a); the simulation results of the corresponding normalized intensity distribution in a logarithmic scale showing a large extent of the attenuated field (b). The micro-resonator cross-section is indicated by gray lines [59]. Used under terms of the CC-BY license. Copyright 2020. Published by Sensors.

Now, there is a discussion about the optimal material for the prong as a part of PAD. Silicon is considered as the best choice for such devices due to better integration with complementary metal-oxide semiconductor-based electronics and optics elements, for example, lasers compared to quartz material [40]. Silicon-based micro-electromechanical systems (MEMS) use piezoelectric, piezoresistive, or capacitive effects. The piezoresistivity is also a property of semiconductors or metals. The capacitive effect is considered as more suitable for the cantilever resonator fabrication compared to piezoelectric one because it is not necessary to deposit a conducting layer on the cantilever. But, capacity response is proportional to the cantilever surface, which causes viscous damping to increase and PAD sensitivity to decrease [40,61,62]. A variant of a capacitive cantilever sensor implementation is shown in Figure 7.

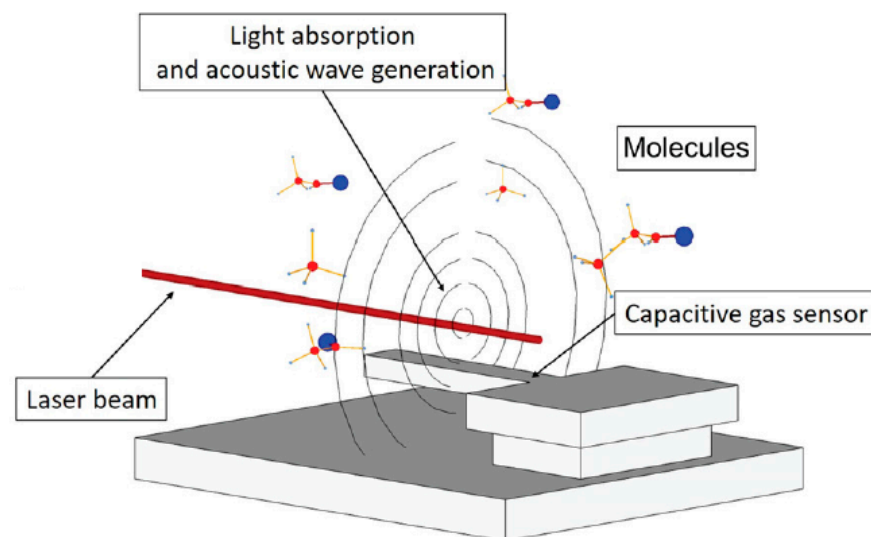


**Figure 7.** A variant of a capacitive cantilever sensor implementation [63]. Used under terms of the license 5573380441735. Copyright 2019. Published by AIP.

A very fruitful idea is to use an optical interferometer for the measurement of cantilever vibrations that provides a high sensitivity to small spatial shifts of a reflecting surface and a fast response. Glauvitz N.E. and co-authors [64] created and tested a MEMS cantilever pressure-sensor for THz spectroscopy. The THz source power was varied in the 0.6–1.4 mW range and the tuning frequency range was 0.250–0.375 THz. The idea of the photoacoustic signal detection using an “optical microphone” implemented by the authors is shown in

Figure 8. A He–Ne laser beam was focused on the cantilever. The gold-plated surface of the cantilever, facing away from the absorbing chamber, reflected the laser beam through a glass window. The deflection of the cantilever caused the deflection of the reflected beam, which was then cut off by the diaphragm located in front of the optical detector. The attenuation is dependent on the deviation of the cantilever. The estimated sensitivity of this detector was  $6.2 \times 10^{-5} \text{ cm}^{-1}/\text{Hz}^{1/2}$ . At 30 mTorr, when the absorption line predominantly has Doppler broadening, the Q-factor was approximately equal to 5000. The effective stiffness of the cantilever used in this experiment was estimated to be 1.3 N/m at a resonant frequency of 626 Hz. The analogous scheme was implemented in the IR spectral range [65]. A commercial version of such an optical cantilever MEMS microphone is produced by Gasera Ltd. (Finland). The comparative experimental study of interferometric and piezoelectric systems of prong vibrations showed that the efficiency of every method depends on the QTF geometry optimization for the specific method of acoustic wave registration [66].

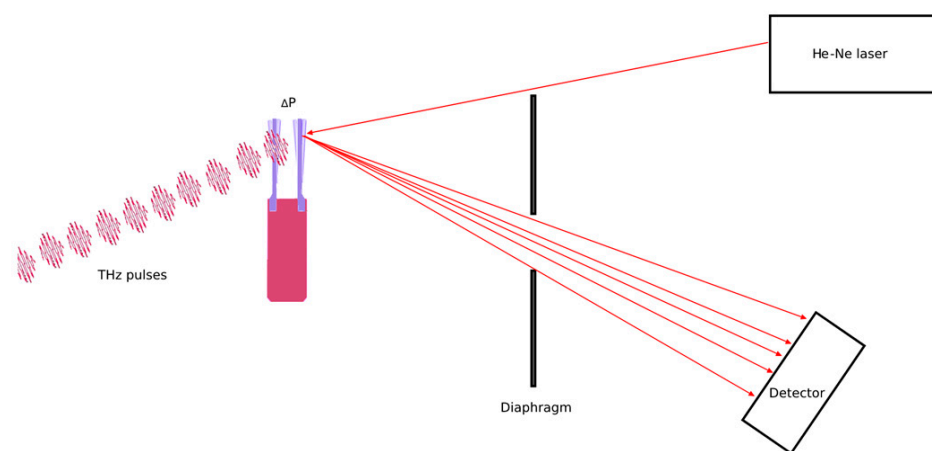


**Figure 8.** The idea of an “optical microphone” for detection of QTF vibrations.

A possible way of improving QTF efficiency is associated with the variation of its prongs’ shape. The analysis of effect of quartz cantilever geometry is on the average strain, the internal strain energy, and the stress distribution over the surface when a cantilever oscillates was conducted [67]. The authors showed that stress distribution over the length of a triangular cantilever is more compared to a rectangular one.

Wavelength modulation absorption spectroscopy is one to two orders of magnitude more sensitive compared to conventional Bouguer’s law-based absorption spectroscopy [68]. In the wavelength modulation spectroscopy, the optical radiation carrier frequency  $\nu(t)$  varies in time so that

$$\nu(t) = \nu_s + \delta\nu \cdot \cos(\omega t) \quad (8)$$

where  $\nu_s$  is the central frequency,  $\delta\nu$  is the frequency modulation depth, and  $\omega$  is the frequency of modulation. Using a lock-in-amplifier linked to the modulation frequency allows restoring various harmonics of the detected signal.

A QEPA system equipped with a Nanoplus Interband QCL ( $\lambda = 3345 \text{ nm}$ ) that has maximum power of  $\sim 8 \text{ mW}$  and a standard 32 kHz QTF coupled with a pair of optimized resonator tubes was created [44]. The authors implemented a  $2f$ -wavelength modulation (WM) method for absorption spectrum detection based on the laser radiation wavelength modulation with a frequency of  $f_0/2$  and the registration of the  $f_0$ -oscillating component of the spectrophone output signal. The wavelength modulation technique allows for improving essentially the signal-to-noise-ratio. The same approach was used for molecular oxygen detection [69]. A detection limit of 13 ppm was reached.

### 3. THz QEPAS Applications

The combination of QTF with a modern THz QCL with a radiation power more than 100 mW [70] would make it possible to detect molecules, such as HF, H<sub>2</sub>S, OH, NH<sub>3</sub>, HCN, etc., up to a concentration range of the order of ppt, when absorption line intensities of more than 10<sup>-19</sup> cm/mol are used. When using similar QCL at a frequency of 3.9 THz, the CH<sub>3</sub>OH detection limit of 160 ppb was achieved with an integration time of 30 s [71].

Sensors based on photo-mixing in the spectral range of 0.5–1.5 THz were created, which allowed detecting HCN, CO, and H<sub>2</sub>CO with a sensitivity of 9 ppm, 0.1%, and 114 ppm, respectively [72]. CH<sub>3</sub>OH sensors were also developed, using THz laser pulses, with an equivalent noise concentration of several ppm [73]. The detection of methyl chloride at the ppm level was conducted using a THz spectrometer with a long base [74].

Sampaolo A. and co-authors [75] created a QEPAS with liquid nitrogen-cooled THz QCL to detect hydrogen sulfide (H<sub>2</sub>S). The detector was a special QTF with a large distance between the prongs connecting with acoustic resonator tubes. A studied H<sub>2</sub>S rotational transition occurs at 2.87 THz (95.626 cm<sup>-1</sup>) with a line intensity of 5.53 × 10<sup>-20</sup> cm/mol. The peak power of THz QCL was 150 mW at a temperature of 81 K, the pulse duration was equal to 1 μs, and a repetition frequency was 15.8 kHz. The H<sub>2</sub>S detection sensitivity was 360 ppm at a gas pressure of 60 Torr and an integration time of 10 s. The scheme of the experimental setup is shown in Figure 9.

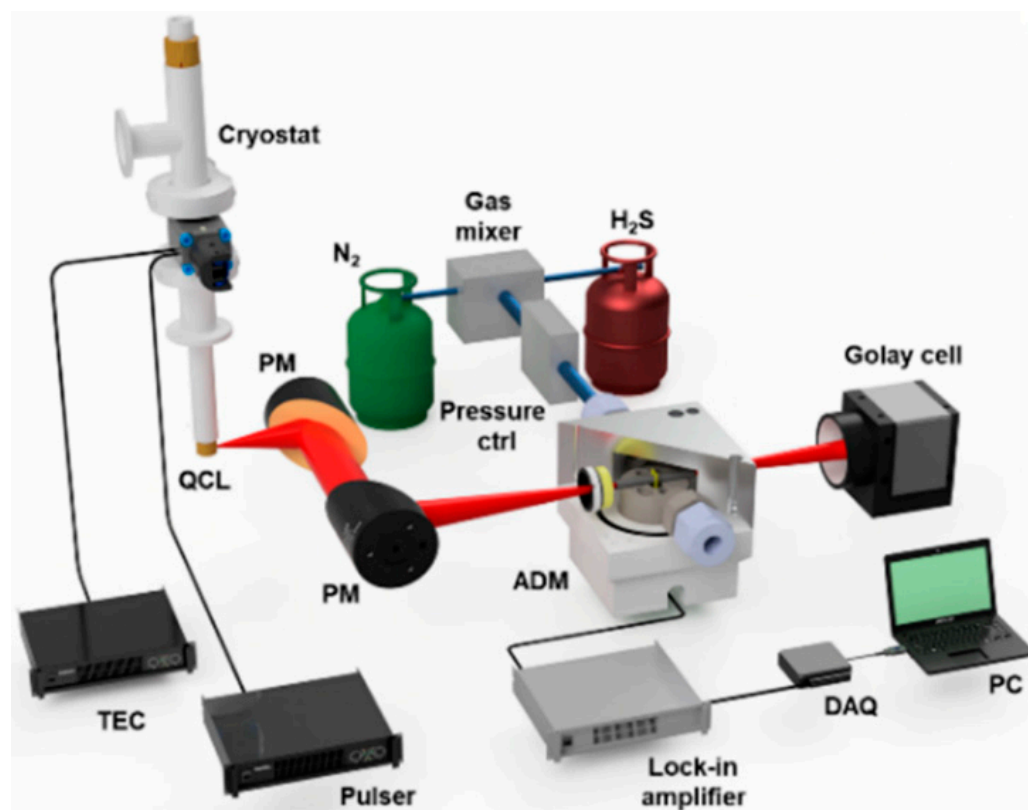


**Figure 9.** The QEPAS sensor scheme. TEC—the thermoelectric cooler; pressure ctrl—the pressure regulator; PM—the parabolic mirror; ADM—the acoustic detection module; DAQ—the data collection board; PC—a personal computer [75]. Used under terms of the CC-BY-NC-ND 4.0 license 5570580201342. Copyright 2021. Published by Photoacoustics.

A THz QCL was used with a lattice coupler for efficient transmission of the THz radiation and a distributed Bragg reflector for single-mode operation. The pulse frequency and spectral width were set in an external signal generator that drives the pulse generator. A Goly cell (Microtech) was used to measure optical power. The QCL radiation spectra were recorded using a Fourier interferometer (Bruker 80 V) with a resolution of 0.1 cm<sup>-1</sup>.

By adjusting the laser current from 3 to 4.1 A, which corresponds to a total wavelength adjustment of  $\sim 0.07 \text{ cm}^{-1}$ , a complete scan of the  $1f$ -QEPAS signal through the  $\text{H}_2\text{S}$  absorption line was recorded. The signal measured for 20 ppm and 100 ppm of  $\text{H}_2\text{S}$  in  $\text{N}_2$  is shown in Figure 10.

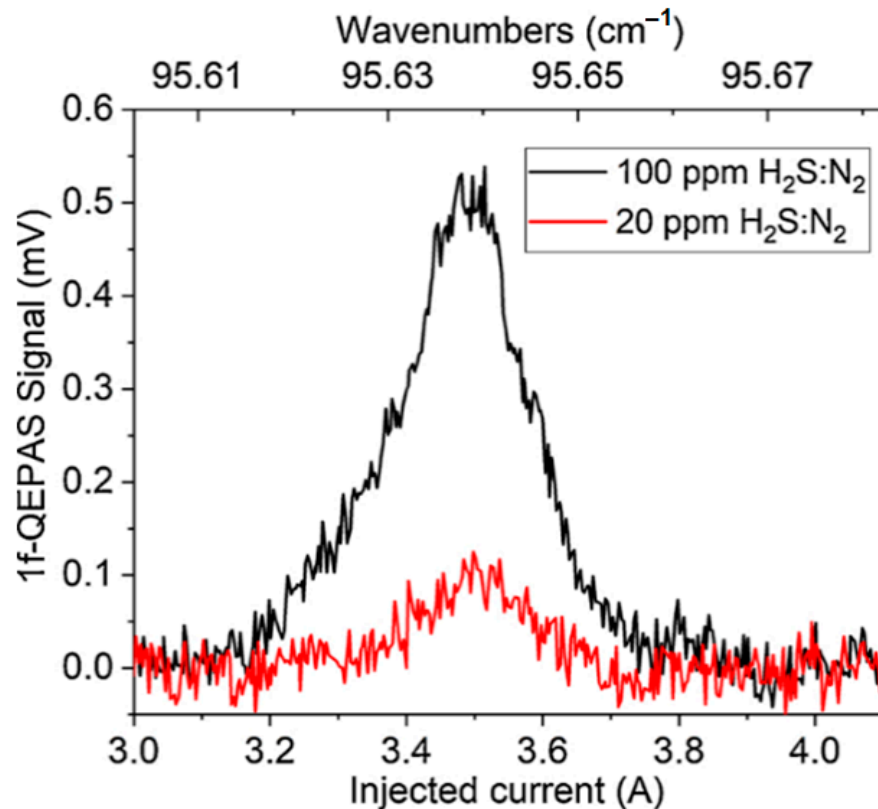


**Figure 10.**  $1f$ -QEPAS signals for a mixture of 100 ppm and 20 ppm  $\text{H}_2\text{S}$  in  $\text{N}_2$  [75]. Used under terms of the CC-BY-NC-ND 4.0 license 5570580201342. Copyright 2021. Published by Photoacoustics.

The main source of a noise in QEPAS is a thermal noise. The latter for a QTF can be expressed in terms of root mean square (RMS) voltage noise

$$\sqrt{V_{rms}^2} = R_g \sqrt{\frac{4k_b T}{R}} \sqrt{\Delta f} \tag{9}$$

where  $k_b$  is the Boltzmann constant,  $T$  is the temperature of the QTF,  $R_g$  is the nominal value of the feedback resistor of the operational amplifier,  $\Delta f$  is the detection bandwidth, and  $R$  is the QTF resistance [46]. According to data shown in Figure 9, for the 20 ppm mixture, a signal-to-noise ratio was about 8, which corresponds to a minimum detection limit of  $\sim 2.5$  ppm with an integration time of 300 ms. To determine how the sensitivity of the QEPAS sensor improves as the integration time increases, an Allan–Werle deviation analysis of the experimental data can be performed. This approach allows also for establishing the main sources of noise of the experimental setup [76]. For example, the minimum detection limit was shown to decrease from 1.6 to 0.53 ppm when the integration time increases from 0.1 to 10 s [75].

Zifarelli A. and co-authors [77] created a THz QEPAS based on a QTF with a distance between the prongs of 1.5 mm for  $\text{H}_2\text{S}$  detection. The experimental setup used pulsed THz QCL and was the same as in [78]. This QCL was placed inside a cryostat with liquid nitrogen, equipped with windows made of polymethylpentene. Fitting the QTF resonance curve by the Lorentz profile gave the following estimates of the resonant frequency:  $f_0 = 15,831.1 \text{ Hz}$  and a Q-factor of 25,400 at 60 Torr. The piezo-current generated by the QTF was converted into a voltage signal using a trans-impedance amplifier ( $R_{fb} = 10 \text{ M}\Omega$ ) and then

fed to a Stanford SR830 synchronous amplifier for demodulation. The QEPAS concentration sensitivity was in the ppb range.

The authors of [76] compared the potential limit of detection of the same molecular component in the THz and IR spectral ranges. The experimental absorption coefficients of the H<sub>2</sub>S in the THz range were two orders of magnitude higher compared to the strongest bands in the mid-IR range. The strongest absorption peak of 95.626 cm<sup>-1</sup> corresponds to the absorption coefficient of 3 cm<sup>-1</sup> and the line strength of 5.53 × 10<sup>-20</sup> cm/mol.

Wilke I. and co-authors [79] described the implementation of a THz spectrometer operating in the 220–330 GHz spectral range. THz waves were generated using an electronic source that included a frequency multiplication chain combined with a GHz signal generator. The THz waves were collimated with a Teflon lens, passed through a cuvette made of high-density polyethylene with windows at an angle of 45° containing the gas sample of interest (path length 21.59 cm), and focused on an electronic detector. The authors used a commercial detector on a Schottky diode and a detector on a dual field-effect transistor monolithically integrated with an antenna [80]. Rotational absorption spectra were registered for four nitrogen-containing compounds of industrial importance (nitrous oxide, acetonitrile, nitric acid, and nitromethane) at pressures from 0.25 to 16 Torr. The authors demonstrated the ability of the selective measurement of these compounds with detection limits of 10<sup>12</sup>–10<sup>13</sup> cm<sup>-3</sup> molecules per meter of path length in pure conditions and 5–1000 ppm per meter of path length for dilute in the air gases at 1 atm.

The minimum detection limit and NNEA of the most effective QEPAS sensors operating in the near–medium IR and THz spectral ranges are shown in Table 1. In the last two rows, a comparison is highlighted between the first THz sensor operating in continuous mode and the sensor presented in [75]. The near-IR sensor had a detection limit below ppm, using the very high power provided by an erbium-doped fiber connected to a laser diode. However, photo-thermal noise caused by the powerful tails of the laser irradiating the spectrophone affected the NNEA. The latter was ~10<sup>-8</sup> cm<sup>-1</sup>·W/√Hz. Currently, the NNEA~8.9 × 10<sup>-12</sup> cm<sup>-1</sup> W/√Hz for H<sub>2</sub>S detection was achieved [81].

In addition, unlike sinusoidal wavelength modulation (see Equation (8)), in which the spectrum of the generated acoustic signal consists of the modulation frequency  $f_{mod}$  and its weak sub-harmonics, the acoustic spectrum of a sequence of pulses with a fast rise and decay consists of many odd harmonics. If we divide the cross-section of the beam into a series of concentric thin rings, then each ring generates an outgoing cylindrical sound wave, and each wave reaches the QTF prong at different times. Thus, the duration  $T_s$  of the resulting primary sound pulse on the QTF wave is  $T_s = T_H + r/v_s$ , where  $T_H$  is the duration of the thermal pulse, which is more than 1 μs,  $v_s$  is the speed of sound (~340 m/s), and  $r$  is the acoustic wave propagation distance. The strongest harmonic component of  $f_{max}$  will be found at  $\sim(T_H + r/v_s)^{-1}$ . A rough calculation gives  $f_{max} \sim 300$  kHz, which does not affect the overall QEPAS signal. At a laser repetition rate of the order of kHz, only a small part of the total sound pressure contributes to the main component, thus affecting the efficiency of sound detection.

**Table 1.** Comparison of high-performance H<sub>2</sub>S QEPAS sensors, from near IR to THz [75]. Used under terms of the CC-BY-NC-ND 4.0 license 5570580201342. Copyright 2021. Published by Photoacoustics.

Spectral Range	Laser Source and Power	Configuration of the Acoustic Detection Module, Acoustic Resonance Frequency; on/off-Beam Scheme	Wavelength (μm)	Absorption Line Strength (cm/mol)	NNEA (cm <sup>1</sup> ·W/√Hz)	Minimum Detection Limit at ~10 s Averaging
Near IR	Fiber-reinforced laser diode, 1500 mW	Adjustable QTF resonator, 7.2 kHz, on-beam	1.5	$1.5 \times 10^{-23}$	$1.3 \times 10^{-8}$	150 ppb
Medium IR	External resonator of a quantum cascade laser, 118 mW, constant power	Standard QTF resonator, 32 kHz, off-beam	8.1	$7.77 \times 10^{-23}$	$3.05 \times 10^{-9}$	40 ppb
THz	Fabry–Perot quantum cascade laser, 0.24 mW, constant power	Tunable QTF resonator, 2.8 kHz, on-beam	103 (2.91 THz)	$1.13 \times 10^{-23}$	$4.4 \times 10^{-10}$	20 ppm
THz	Fabry–Perot quantum cascade laser, 150 mW, pulsed	Adjustable QTF resonator, 15.8 kHz, on-beam	104.6 (2.87 THz)	$5.53 \times 10^{-23}$	$3.1 \times 10^{-8}$	360 ppb

#### 4. Conclusions

A quartz-enhanced photoacoustic spectroscopy allows achieving acceptable sensitivity in the THz spectral range with several tens of mW power THz wave sources. The Q-factor of photo-acoustic detectors with a quartz tuning fork can reach several tens of thousands. A huge advantage of quartz tuning fork detectors is that they can operate in an open space that simplifies their operation in a wide spectral range. It opens a way of creation of spectrometers operating in the THz–IR range.

A known drawback of PAS is that the signal-to-noise ratio falls at very low pressures, which is sometimes necessary to reduce the absorption line impact broadening and achieve high spectral resolution. This issue can be solved using the method of computer super-resolution reconstruction developed by us, which improves spectral resolution of the experimental spectra [82].

The increase in PAS sensitivity is possible by combining several of the following resonances [83]:

- Resonant absorption by a target gas component in a sample when the optical radiation source wavelength coincides with a central wavelength of an absorption line of this component;
- Focusing the optical radiation in a small volume;
- Mechanical resonance in an acoustic transducer when a frequency of amplitude of wavelength modulation of the optical radiation coincides with a resonance frequency of the transducer.

The control of the simultaneous fulfillment of all these conditions is a nontrivial task due to influence of physical parameters of the studied gas sample. The central wavelength and shape of the absorption line depends on the studied gas sample temperature, pressure, and buffer gas (collision partner) properties (see, for example, Equation (7)). Acoustic resonances depend on the temperature [84,85], humidity [86], and the gas sample composition [87,88].

The condition of exact resonance of optical radiation absorption can be checked when the optical radiation source wavelength is tuned in the spectral interval of a measured absorption line. For example, it can be implemented by the method of scanned-wavelength absorption spectroscopy [89–91]. The temperature effects can be essentially decreased by thermostating. A high humidity can affect dramatically on QTF acoustic resonance. It especially concerns commercial devices [92].

The frequency of acoustic resonances in IR PADs can be tested using an additional speaker placed in the measurement chamber and controlled by a sound generator. This variant was used in the IR OPO-based PAS device “LaserBreeze” [8]. Also, a variation of modulation frequency of an optical radiation source amplitude or frequency allows checking the conditions of acoustic resonances by achieving the maximal electrical signal on the detector output.

**Author Contributions:** Conceptualization, Y.V.K. and A.V.B.; formal analysis, D.R.M., M.Y.S. and A.P.V.; writing—original draft preparation, D.R.M., M.Y.S. and A.P.V.; writing—review and editing, Y.V.K. and A.V.B.; supervision, Y.V.K. All authors have read and agreed to the published version of the manuscript.

**Funding:** The research was supported by the Grant of the Russian Ministry of Education and Science (Agreement No. 075-15-2021-1412 (13.2251.21.0128) dated 12/23/2021, unique contract identifier RF 2251.62321X0012).

**Institutional Review Board Statement:** Not applicable.

**Informed Consent Statement:** Not applicable.

**Data Availability Statement:** The data presented in this study are available on request from the corresponding author. The data are not publicly available due to privacy.

**Conflicts of Interest:** The authors declare no conflict of interest.

## References

1. Wang, F.; Cheng, Y.; Xue, Q.; Wang, Q.; Liang, R.; Wu, J.; Sun, J.; Zhu, C.; Li, Q. Techniques to Enhance the Photoacoustic Signal for Trace Gas Sensing: A Review. *Sens. Actuators A Phys.* **2022**, *345*, 113807. [CrossRef]
2. Kistenev, Y.V.; Cuisset, A.; Romanovskii, O.A.; Zherdeva, A.V. A Study of Trace Atmospheric Gases at the Water–Atmosphere Interface Using Remote and Local IR Laser Gas Analysis: A Review. *Atmos. Ocean. Opt.* **2022**, *35*, S1, S17–S29. [CrossRef]
3. The Hitran Database. Available online: <https://hitran.org/> (accessed on 28 June 2023).
4. GEISA—Spectroscopic Database. Available online: <https://geisa.aeris-data.fr> (accessed on 28 June 2023).
5. Kistenev, Y.V.; Cuisset, A.; Hindl, F.; Raspopin, G.K.; Vax, V.L.; Domracheva, E.G.; Chernyaeva, M.B.; Karapuzikov, A.I. The Potential of Compact Sub-THz Band Spectrometers Based on Cascade Frequency Multiplication for Local Environmental Monitoring of the Atmosphere. *Radiophys. Quantum Electron.* **2023**, in print. [CrossRef]
6. Cuisset, A.; Hindle, F.; Mouret, G.; Bocquet, R.; Bruckhuisen, J.; Decker, J.; Pienkina, A.; Bray, C.; Fertein, É.; Boudon, V. Terahertz Rotational Spectroscopy of Greenhouse Gases Using Long Interaction Path-Lengths. *Appl. Sci.* **2021**, *11*, 1229. [CrossRef]
7. Zeninari, V.; Vallon, R.; Risser, C.; Parvitte, B. Photoacoustic Detection of Methane in Large Concentrations with a Helmholtz Sensor: Simulation and Experimentation. *Int. J. Thermophys.* **2016**, *37*, 7. [CrossRef]
8. Karapuzikov, A.A.; Sherstov, I.V.; Kolker, D.B.; Karapuzikov, A.I.; Kistenev, Y.V.; Kuzmin, D.A.; Shtyrov, M.Y.; Dukhovnikova, N.Y.; Zenov, K.G.; Boyko, A.A.; et al. LaserBreeze Gas Analyzer for Noninvasive Diagnostics of Air Exhaled by Patients. *Phys. Wave Phenom.* **2014**, *22*, 189–196. [CrossRef]
9. Miklós, A.; Hess, P.; Bozóki, Z. Application of Acoustic Resonators in Photoacoustic Trace Gas Analysis and Metrology. *Rev. Sci. Instrum.* **2001**, *72*, 1937–1955. [CrossRef]
10. Raspopin, G.K.; Makashev, D.R.; Borisov, A.V.; Kistenev, Y.V. Analysis of High-Frequency Acoustic Resonances of an Opto-Acoustic Detector with Differential Helmholtz Resonators. *Opt. Spectrosc.* **2022**, *130*, 278–283. [CrossRef]
11. Kolker, D.B.; Pustovalova, R.V.; Starikova, M.K.; Karapuzikov, A.I.; Karapuzikov, A.A.; Kuznetsov, O.M.; Kistenev, Y.V. Optical Parametric Oscillator within 2.4–4.3 Mm Pumped with a Nanosecond Nd:YAG Laser. *Atmos. Ocean. Opt.* **2012**, *25*, 77–81. [CrossRef]
12. Olvera, A.D.J.F.; Lu, H.; Gossard, A.C.; Preu, S. Continuous-Wave 1550 Nm Operated Terahertz System Using ErAs:In(Al)GaAs Photo-Conductors with 52 DB Dynamic Range at 1 THz. *Opt. Express.* **2017**, *25*, 29492. [CrossRef]
13. Zhu, J.; Qiao, D.; Jones, A.; Zhang, B.; Li, K.; Copner, N. 1.7 THz Tuning Range Pivot-Point-Independent Mode-Hop-Free External Cavity Diode Laser. *Opt. Express.* **2023**, *31*, 3970. [CrossRef] [PubMed]
14. Hoppe, M.; Schmidtman, S.; Aßmann, C.; Honsberg, M.; Milde, T.; Schanze, T.; Sacher, J.R.; Gu-Stoppel, S.; Senger, F. High Speed External Cavity Diode Laser Concept Based on a Resonantly Driven MEMS Scanner for the Mid-Infrared Region. *Appl. Opt.* **2021**, *60*, 92. [CrossRef]
15. Bayrakli, I. Tunable Double-Mode Sensor for Multi-Gas Detection Based on the External-Cavity Diode Laser. *Appl. Opt.* **2018**, *57*, 4039. [CrossRef] [PubMed]
16. Takida, Y.; Ikeo, T.; Nawata, K.; Wada, Y.; Higashi, Y.; Minamide, H. Terahertz Differential Absorption Spectroscopy Using Multifurcated Subnanosecond Microchip Laser. *Appl. Phys. Lett.* **2019**, *115*, 121102. [CrossRef]
17. Khan, M.S.; Keum, C.; Xiao, Y.; Isamoto, K.; Nishiyama, N.; Toshiyoshi, H. MEMS-VCSEL as a Tunable Light Source for OCT Imaging of Long Working Distance. *J. Opt. Microsyst.* **2021**, *1*, 1–16. [CrossRef]
18. Shi, G.; Wang, W.; Zhang, F. Precision Improvement of Frequency-Modulated Continuous-Wave Laser Ranging System with Two Auxiliary Interferometers. *Opt. Commun.* **2018**, *411*, 152–157. [CrossRef]
19. Pongrac, B.; Donlagic, D.; Njegovec, M.; Gleich, D. THz Signal Generator Using a Single DFB Laser Diode and the Unbalanced Optical Fiber Interferometer. *Sensors* **2020**, *20*, 4862. [CrossRef]
20. Chi, M.; Jensen, O.B.; Petersen, P.M. High-Power Dual-Wavelength External-Cavity Diode Laser Based on Tapered Amplifier with Tunable Terahertz Frequency Difference. *Opt. Lett.* **2011**, *36*, 2626. [CrossRef]
21. Wang, J.; Tu, T.; Zhang, F.; Shen, F.; Xu, J.; Cao, Z.; Gao, X.; Plus, S.; Chen, W. External-Cavity Diode Laser-Based near-Infrared Broadband Laser Heterodyne Radiometer for Remote Sensing of Atmospheric CO<sub>2</sub>. *Opt. Express.* **2023**, *31*, 9251. [CrossRef]
22. Lu, Y.; Zhang, W.; Fan, J.; Zhou, X.; Wang, Y.; Qu, H.; Zheng, W. High-Power Tunable Dual-Wavelength Diode Laser with a Composite External Cavity. *Opt. Lett.* **2022**, *47*, 2486. [CrossRef]
23. Mine, S.; Kawase, K.; Murate, K. Real-Time Wide Dynamic Range Spectrometer Using a Rapidly Wave-length-Switchable Terahertz Parametric Source. *Opt. Lett.* **2021**, *46*, 2618. [CrossRef] [PubMed]
24. Zheng, Y.; Kurita, T.; Sekine, T.; Kato, Y.; Kawashima, T. Tunable Continuous-Wave Dual-Wavelength Laser by External-Cavity Superluminescent Diode with a Volume Bragg Grating and a Diffraction Grating. *Appl. Phys. Lett.* **2016**, *109*. [CrossRef]
25. Yao, Y.; Hoffman, A.J.; Gmachl, C.F. Mid-Infrared Quantum Cascade Lasers. *Nat. Photonics* **2012**, *6*, 432–439. [CrossRef]
26. Deutsch, C.; Detz, H.; Zederbauer, T.; Krall, M.; Brandstetter, M.; Andrews, A.M.; Klang, P.; Schrenk, W.; Strasser, G.; Unterrainer, K. InGaAs/GaAsSb/InP Terahertz Quantum Cascade Lasers. *J. Infrared. Millim Terahertz Waves* **2013**, *34*, 374–385. [CrossRef]
27. Vurgaftman, I.; Canedy, C.L.; Kim, C.S.; Kim, M.; Bewley, W.W.; Lindle, J.R.; Abell, J.; Meyer, J.R. Mid-Infrared Interband Cascade Lasers Operating at Ambient Temperatures. *New J. Phys.* **2009**, *11*, 125015. [CrossRef]
28. Williams, B.S. Terahertz Quantum-Cascade Lasers. *Nat. Photonics* **2007**, *1*, 517–525. [CrossRef]

29. Fujita, K.; Hayashi, S.; Ito, A.; Hitaka, M.; Dougakiuchi, T. Sub-Terahertz and Terahertz Generation in Long-Wavelength Quantum Cascade Lasers. *Nanophotonics* **2019**, *8*, 2235–2241. [[CrossRef](#)]
30. Lindner, S.; Hayden, J.; Schwaighofer, A.; Wolflehner, T.; Kristament, C.; González-Cabrera, M.; Zlabinger, S.; Lendl, B. External Cavity Quantum Cascade Laser-Based Mid-Infrared Dispersion Spectroscopy for Qualitative and Quantitative Analysis of Liquid-Phase Samples. *Appl. Spectrosc.* **2020**, *74*, 452–459. [[CrossRef](#)]
31. Scheuermann, J.; Kluczynski, P.; Siembab, K.; Straszewski, M.; Kaczmarek, J.; Weih, R.; Fischer, M.; Koeth, J.; Schade, A.; Höfling, S. Interband Cascade Laser Arrays for Simultaneous and Selective Analysis of C1–C5 Hydrocarbons in Petrochemical Industry. *Appl. Spectrosc.* **2021**, *75*, 336–342. [[CrossRef](#)]
32. Giraud, E.; Demolon, P.; Gresch, T.; Urio, L.; Muller, A.; Maulini, R. Room-Temperature Continuous-Wave External Cavity Interband Cascade Laser Tunable from 3.2 to 3.6 Mm. *Opt. Express.* **2021**, *29*, 38291. [[CrossRef](#)]
33. Cherotchenko, E.D.; Dudelev, V.V.; Mikhailov, D.A.; Losev, S.N.; Babichev, A.V.; Gladyshev, A.G.; Novikov, I.I.; Lutetskiy, A.V.; Veselov, D.A.; Slipchenko, S.O.; et al. Observation of Long Turn-On Delay in Pulsed Quantum Cascade Lasers. *J. Light. Technol.* **2022**, *40*, 2104–2110. [[CrossRef](#)]
34. Vanier, F.; Parrot, A.; Padioleau, C.; Blouin, A. Mid-Infrared Reflectance Spectroscopy Based on External Cavity Quantum Cascade Lasers for Mineral Characterization. *Appl. Spectrosc.* **2022**, *76*, 361–368. [[CrossRef](#)] [[PubMed](#)]
35. Ma, Y. Review of Recent Advances in QEPAS-Based Trace Gas Sensing. *Appl. Sci.* **2018**, *8*, 1822. [[CrossRef](#)]
36. Spagnolo, V.; Patimisco, P.; Borri, S.; Sampaolo, A.; Scamarcio, G.; Vitiello, M.S.; Beere, H.E.; Ritchie, D.A. THz Quartz-Enhanced Photoacoustic Sensor Employing a Quantum Cascade Laser Source. *Proc. SPIE* **2013**, *8993*, 899320.
37. Borri, S.; Patimisco, P.; Sampaolo, A.; Beere, H.E.; Ritchie, D.A.; Vitiello, M.S.; Scamarcio, G.; Spagnolo, V. Terahertz Quartz Enhanced Photo-Acoustic Sensor. *Appl. Phys. Lett.* **2013**, *103*, 021105. [[CrossRef](#)]
38. Spagnolo, V.; Borri, S.; Patimisco, P.; Sampaolo, A.; Calabrese, P.P.; Beere, H.E.; Ritchie, D.A.; Vitiello, M.S.; Scamarcio, G. THz Quantum Cascade Laser-Based Quartz Enhanced Photo-Acoustic Sensor. In Proceedings of the 2013 38th International Conference on Infrared, Millimeter, and Terahertz Waves (IRMMW-THz), Mainz, Germany, 1–6 September 2013; pp. 1–3.
39. Elia, A.; Lugarà, P.M.; Di Franco, C.; Spagnolo, V. Photoacoustic Techniques for Trace Gas Sensing Based on Semiconductor Laser Sources. *Sensors* **2009**, *9*, 9616–9628. [[CrossRef](#)]
40. Trzpil, W.; Maurin, N.; Rousseau, R.; Ayache, D.; Vicet, A.; Bahriz, M. Analytic Optimization of Cantilevers for Photoacoustic Gas Sensor with Capacitive Transduction. *Sensors* **2021**, *21*, 1489. [[CrossRef](#)]
41. Patimisco, P.; Sampaolo, A.; Giglio, M.; dello Russo, S.; Mackowiak, V.; Rossmadl, H.; Cable, A.; Tittel, F.K.; Spagnolo, V. Tuning forks with optimized geometries for quartz-enhanced photoacoustic spectroscopy. *Opt. Express* **2019**, *27*, 1401. [[CrossRef](#)]
42. Glauvitz, N.E.; Coutu, R.A.; Medvedev, I.R.; Petkie, D.T. Terahertz Photoacoustic Spectroscopy Using an MEMS Cantilever Sensor. *J. Microelectromechanical Syst.* **2015**, *24*, 216–223. [[CrossRef](#)]
43. Sampaolo, A.; Patimisco, P.; Giglio, M.; Zifarelli, A.; Wu, H.; Dong, L.; Spagnolo, V. Quartz-Enhanced Photo-acoustic Spectroscopy for Multi-Gas Detection: A Review. *Anal. Chim. Acta* **2022**, *1202*, 338894. [[CrossRef](#)]
44. Menduni, G.; Zifarelli, A.; Sampaolo, A.; Patimisco, P.; Giglio, M.; Amoroso, N.; Wu, H.; Dong, L.; Bellotti, R.; Spagnolo, V. High-Concentration Methane and Ethane QEPAS Detection Employing Partial Least Squares Regression to Filter out Energy Relaxation Dependence on Gas Matrix Composition. *Photoacoustics* **2022**, *26*, 100349. [[CrossRef](#)] [[PubMed](#)]
45. Glauvitz, N.; Coutu, R.A.; Medvedev, I.R.; Petkie, D.T. MEMS-Based Terahertz Photoacoustic Chemical Sensing System. In *Progresses in Chemical Sensor*; InTech: Rijeka, Croatia, 2016; Volume 2, pp. 11–36. [[CrossRef](#)]
46. Patimisco, P.; Borri, S.; Sampaolo, A.; Beere, H.E.; Ritchie, D.A.; Vitiello, M.S.; Scamarcio, G.; Spagnolo, V. A Quartz Enhanced Photo-Acoustic Gas Sensor Based on a Custom Tuning Fork and a Terahertz Quantum Cascade Laser. *Analyst* **2014**, *139*, 2079–2087. [[CrossRef](#)] [[PubMed](#)]
47. Spagnolo, V.; Patimisco, P.; Sampaolo, A.; Giglio, M.; Vitiello, M.S.; Scamarcio, G.; Tittel, F.K. New Developments in THz Quartz Enhanced Photoacoustic Spectroscopy. In *Terahertz Emitters, Receivers, and Applications VII*; SPIE: Bellingham, WA, USA, 2016; Volume 9934, p. 99340. [[CrossRef](#)]
48. Patimisco, P.; Scamarcio, G.; Tittel, F.; Spagnolo, V. Quartz-Enhanced Photoacoustic Spectroscopy: A Review. *Sensors* **2014**, *14*, 6165–6206. [[CrossRef](#)]
49. Duquesnoy, M.; Aoust, G.; Melkonian, J.-M.; Lévy, R.; Raybaut, M.; Godard, A. Quartz Enhanced Photoacoustic Spectroscopy Based on a Custom Quartz Tuning Fork. *Sensors* **2019**, *19*, 1362. [[CrossRef](#)] [[PubMed](#)]
50. Sadiq, I.; Mikkonen, T.; Vainio, M.; Toivonen, J.; Foltynowicz, A. Optical Frequency Comb Photoacoustic Spectroscopy. *Phys. Chem. Chem. Phys.* **2018**, *20*, 27849–27855. [[CrossRef](#)]
51. McNaghten, E.D.; Grant, K.A.; Parkes, A.M.; Martin, P.A. Simultaneous Detection of Trace Gases Using Mul-tiplexed Tunable Diode Lasers and a Photoacoustic Cell Containing a Cantilever Microphone. *Appl. Phys. B* **2012**, *107*, 861–871. [[CrossRef](#)]
52. Dong, L.; Kosterev, A.A.; Thomazy, D.; Tittel, F.K. QEPAS spectrophones: Design, optimization, and performance. *Appl. Phys. B* **2010**, *100*, 627–635. [[CrossRef](#)]
53. Verstuyft, M.; Akiki, E.; Walter, B.; Faucher, M.; Vanwollegem, M.; Kuyken, B. An Integrated Photoacoustic Terahertz Gas Sensor. In Proceedings of the 2019 44th International Conference on Infrared, Millimeter, and Terahertz Waves (IRMMW-THz), Paris, France, 1–6 September 2019; pp. 1–2.
54. Kun, L.; Xiaoyong, G.; Hongming, Y.; Weidong, C.; Weijun, Z.; Xiaoming, G. Off-beam quartz-enhanced photoacoustic spectroscopy. *Opt. Lett.* **2009**, *34*, 1594–1596. [[CrossRef](#)]

55. Köhring, M.; Böttger, S.; Willer, U.; Schade, W. LED-Absorption-QEPAS Sensor for Biogas Plants. *Sensors* **2015**, *15*, 12092–12102. [[CrossRef](#)]
56. Rousseau, R.; Loghmani, Z.; Bahriz, M.; Chamassi, K.; Teissier, R.; Baranov, A.N.; Vicet, A. Off-Beam QEPAS Sensor Using an 11-Mm DFB-QCL with an Optimized Acoustic Resonator. *Opt. Express*. **2019**, *27*, 7435. [[CrossRef](#)]
57. Hellström, J.; Jänes, P.; Elgcróna, G.; Karlsson, H. Compact and Efficient Nanosecond Pulsed Tuneable OPO in the Mid-IR Spectral Range. In Proceedings of the SPIE—The International Society for Optical Engineering, München, Germany, 13–16 May 2013; Volume 8733, p. 87330A. [[CrossRef](#)]
58. Rousseau, R.; Ayache, D.; Maurin, N.; Trzpił, W.; Bahriz, M.; Vicet, A. Monolithic Double Resonator for Quartz Enhanced Photoacoustic Spectroscopy. *Appl. Sci.* **2021**, *11*, 2094. [[CrossRef](#)]
59. Vogt, D.W.; Jones, A.H.; Leonhardt, R. Terahertz Gas-Phase Spectroscopy Using a Sub-Wavelength Thick Ultra-high-Q Microresonator. *Sensors* **2020**, *20*, 3005. [[CrossRef](#)] [[PubMed](#)]
60. Vogt, D.W.; Jones, A.H.; Haase, T.A.; Leonhardt, R. Subwavelength Thick Ultrahigh-Q Terahertz Disc Microresonators. *Photonics Res.* **2020**, *8*, 1183. [[CrossRef](#)]
61. Seoudi, T.; Charensol, J.; Trzpił, W.; Pages, F.; Ayache, D.; Rousseau, R.; Vicet, A.; Bahriz, M. Highly Sensitive Capacitive MEMS for Photoacoustic Gas Trace Detection. *Sensors* **2023**, *23*, 3280. [[CrossRef](#)] [[PubMed](#)]
62. Trzpił, W.; Charensol, J.; Ayache, D.; Maurin, N.; Rousseau, R.; Vicet, A.; Bahriz, M. A Silicon Micromechanical Resonator with Capacitive Transduction for Enhanced Photoacoustic Spectroscopy. *Sens. Actuators B Chem.* **2022**, *353*, 131070. [[CrossRef](#)]
63. Chamassi, K.; Trzpił, W.; Arinero, R.; Rousseau, R.; Vicet, A.; Bahriz, M. Capacitive Silicon Micro-Electromechanical Resonator for Enhanced Photoacoustic Spectroscopy. *Appl. Phys. Lett.* **2019**, *115*, 081106. [[CrossRef](#)]
64. Glauvitz, N.E.; Coutu, R.A.; Petkie, D.T.; Medvedev, I.R. A Micro-Cantilever Based Photoacoustic Detector of Terahertz Radiation for Chemical Sensing. In Proceedings of the 2013 38th International Conference on Infrared, Millimeter, and Terahertz Waves (IRMMW-THz), Mainz, Germany, 1–6 September 2013; pp. 1–3.
65. Adamson, B.D.; Sader, J.E.; Bieske, E.J. Photoacoustic Detection of Gases Using Microcantilevers. *J. Appl. Phys.* **2009**, *106*, 114510. [[CrossRef](#)]
66. Patimisco, P.; Zou, S.; dello Russo, S.; Zifarelli, A.; Sampaolo, A.; Giglio, M.; Rossmadl, H.; Mackowiak, V.; Cable, A.; Iannuzzi, D.; et al. Comparison between interferometric and piezoelectric readout of tuning fork vibrations in quartz-enhanced photoacoustic spectroscopy. *Proc. SPIE* **2020**, *11301*, 113011S. [[CrossRef](#)]
67. Siddiqui, N.A.; Kim, S.-B.; Kim, D.-J.; Overfelt, R.A.; Prorok, B.C. Shape Optimization of Cantilevered Piezoelectric Devices. In *MEMS and Nanotechnology, Volume 5, Proceedings of the 2013 Annual Conference on Experimental and Applied Mechanics*; Springer: Cham, Switzerland, 2014; pp. 43–48. [[CrossRef](#)]
68. Mouret, G.; Guinet, M.; Cuisset, A.; Croize, L.; Eliet, S.; Bocquet, R.; Hindle, F. Versatile Sub-THz Spectrometer for Trace Gas Analysis. *IEEE Sens. J.* **2013**, *13*, 133–138. [[CrossRef](#)]
69. Pohlkötter, A.; Köhring, M.; Willer, U.; Schade, W. Detection of molecular oxygen at low concentrations using quartz enhanced photoacoustic spectroscopy. *Sensors* **2010**, *10*, 8466. [[CrossRef](#)]
70. Williams, B.S.; Kumar, S.; Hu, Q.; Reno, J.L. High-Power Terahertz Quantum-Cascade Lasers. *Electron. Lett.* **2006**, *42*, 89. [[CrossRef](#)]
71. Sampaolo, A.; Patimisco, P.; Giglio, M.; Vitiello, M.; Beere, H.; Ritchie, D.; Scamarcio, G.; Tittel, F.; Spagnolo, V. Improved Tuning Fork for Terahertz Quartz-Enhanced Photoacoustic Spectroscopy. *Sensors* **2016**, *16*, 439. [[CrossRef](#)] [[PubMed](#)]
72. Bigourd, D.; Cuisset, A.; Hindle, F.; Matton, S.; Bocquet, R.; Mouret, G.; Cazier, F.; Dewaele, D.; Nouali, H. Multiple Component Analysis of Cigarette Smoke Using THz Spectroscopy, Comparison with Standard Chemical Analytical Methods. *App. Phys.* **2007**, *86*, 579–586. [[CrossRef](#)]
73. Gerecht, E.; Douglass, K.O.; Plusquellic, D.F. Chirped-Pulse Terahertz Spectroscopy for Broadband Trace Gas Sensing. *Opt. Express*. **2011**, *19*, 8973. [[CrossRef](#)]
74. Harmon, S.A.; Cheville, R.A. Part-per-Million Gas Detection from Long-Baseline THz Spectroscopy. *Appl. Phys. Lett.* **2004**, *85*, 2128–2130. [[CrossRef](#)]
75. Sampaolo, A.; Yu, C.; Wei, T.; Zifarelli, A.; Giglio, M.; Patimisco, P.; Zhu, H.; Zhu, H.; He, L.; Wu, H.; et al. H<sub>2</sub>S Quartz-Enhanced Photoacoustic Spectroscopy Sensor Employing a Liquid-Nitrogen-Cooled THz Quantum Cascade Laser Operating in Pulsed Mode. *Photoacoustics* **2021**, *21*, 100219. [[CrossRef](#)]
76. Giglio, M.; Patimisco, P.; Sampaolo, A.; Scamarcio, G.; Tittel, F.K.; Spagnolo, V. Allan Deviation Plot as a Tool for Quartz Enhanced Photoacoustic Sensors Noise Analysis. *IEEE Trans. Ultrason. Ferroelectr. Freq. Control.* **2016**, *63*, 555. [[CrossRef](#)]
77. Zifarelli, A.; Sampaolo, A.; Patimisco, P.; Giglio, M.; Yu, C.; Zhu, H.; Zhu, H.; Chang, G.; Wang, F.; Chen, J.; et al. N<sub>2</sub>-Cooled THz Quartz-Enhanced Photoacoustic Sensor Operating in Pulsed Mode for Hydrogen Sulfide Detection in the Part-per-Billion Concentration Range. In *Proceedings of the Quantum Sensing and Nano Electronics and Photonics XVII*; Razeghi, M., Lewis, J.S., Khodaparast, G.A., Khalili, P., Eds.; SPIE: Bellingham, WA, USA, 2020; p. 70.
78. Yu, C.; Zhu, H.; Wang, F.; Chang, G.; Zhu, H.; Chen, J.; Chen, P.; Tang, Z.; Lu, W.; Shen, C.; et al. Highly Efficient Power Extraction in Terahertz Quantum Cascade Laser via a Grating Coupler. *Appl. Phys. Lett.* **2018**, *113*, 121114. [[CrossRef](#)]

79. Wilke, I.; Rice, T.E.; Mansha, M.W.; Chowdhury, M.A.Z.; Hella, M.M.; Oehlschlaeger, M.A. Quantitative Gas Spectroscopy in the 220 to 330 GHz Frequency Band Utilizing a Microelectronic Spectrometer. In Proceedings of the 2022 47th International Conference on Infrared, Millimeter and Terahertz Waves (IRMMW-THz), Delft, The Netherlands, 28 August–2 September 2022; pp. 1–2.
80. Mansha, M.W.; Rice, T.E.; Oehlschlaeger, M.A.; Wilke, I.; Hella, M.M. A 220–300 GHz Twin-FET Detector for Rotational Spectroscopy of Gas Mixtures. *IEEE Sens. J.* **2021**, *21*, 4553–4562. [[CrossRef](#)]
81. Zhang, H.; Wang, Z.; Wang, Q.; Borri, S.; Galli, I.; Sampaolo, A.; Patimisco, P.; Spagnolo, V.L.; De Natale, P.; Ren, W. Parts-per-billion-level detection of hydrogen sulfide based on doubly resonant photoacoustic spectroscopy with line-locking. *Photoacoustics* **2023**, *29*, 100436. [[CrossRef](#)]
82. Kistenev, Y.V.; Skiba, V.E.; Prischepa, V.V.; Vrazhnov, D.A.; Borisov, A.V. Super-Resolution Reconstruction of Noisy Gas-Mixture Absorption Spectra Using Deep Learning. *J. Quant. Spectrosc. Radiat. Transf.* **2022**, *289*, 108278. [[CrossRef](#)]
83. Palzer, S. Photoacoustic-Based Gas Sensing: A Review. *Sensors* **2020**, *20*, 2745. [[CrossRef](#)]
84. Niu, M.; Liu, Q.; Liu, K.; Yuan, Y.; Gao, X. Temperature-Dependent Characteristics of a Photoacoustic Detector. *Optik (Stuttg)* **2013**, *124*, 2450–2454. [[CrossRef](#)]
85. Szakáll, M.; Csikós, J.; Bozóki, Z.; Szabó, G. On the Temperature Dependent Characteristics of a Photoacoustic Water Vapor Detector for Airborne Application. *Infrared. Phys. Technol.* **2007**, *51*, 113–121. [[CrossRef](#)]
86. Barreiro, N.; Peuriot, A.; Santiago, G.; Slezak, V. Water-Based Enhancement of the Resonant Photoacoustic Signal from Methane–Air Samples Excited at 3.3 Mm. *Appl. Phys. B* **2012**, *108*, 369–375. [[CrossRef](#)]
87. Barreiro, N.; Vallespi, A.; Santiago, G.; Slezak, V.; Peuriot, A. Influence of Oxygen on the Resonant Photoacoustic Signal from Methane Excited at the  $\nu_3$  Mode. *Appl. Phys. B* **2011**, *104*, 983–987. [[CrossRef](#)]
88. Barreiro, N.; Peuriot, A.; Slezak, V.; Santiago, G. Study of the Dependence of the Photoacoustic Signal Amplitude from Methane on Different Collisional Partners. *Vib. Spectrosc.* **2013**, *68*, 158–161. [[CrossRef](#)]
89. Kistenev, Y.V.; Borisov, A.V.; Vrazhnov, D.A. *Medical Applications of Laser Molecular Imaging and Machine Learning*; SPIE: Bellingham, WA, USA, 2021; ISBN 9781510645356.
90. Kistenev, Y.V.; Borisov, A.V.; Vrazhnov, D.A. Breathomics for Lung Cancer Diagnosis. In *Multimodal Optical Diagnostics of Cancer*; Springer International Publishing: Cham, Switzerland, 2020; pp. 209–243. [[CrossRef](#)]
91. Borisov, A.V.; Syrkina, A.G.; Kuzmin, D.A.; Ryabov, V.V.; Boyko, A.A.; Zaharova, O.; Zasedatel, V.S.; Kistenev, Y. V Application of Machine Learning and Laser Optical-Acoustic Spectroscopy to Study the Profile of Exhaled Air Volatile Markers of Acute Myocardial Infarction. *J. Breath Res.* **2021**, *15*, 027104. [[CrossRef](#)]
92. Ayache, D.; Rousseau, R.; Kniazeva, E.; Charensol, J.; Seoudi, T.; Bahriz, M.; Gouzi, F.; Spagnolo, V.; Vicet, A. Commercial and Custom Quartz Tuning Forks for Quartz Enhanced Photoacoustic Spectroscopy: Stability under Humidity Variation. *Sensors* **2023**, *23*, 3135. [[CrossRef](#)]

**Disclaimer/Publisher’s Note:** The statements, opinions and data contained in all publications are solely those of the individual author(s) and contributor(s) and not of MDPI and/or the editor(s). MDPI and/or the editor(s) disclaim responsibility for any injury to people or property resulting from any ideas, methods, instructions or products referred to in the content.